Summer 8-1-2023

Seismic Analysis of the Upper & Lower Falls of the Yellowstone River

Loring Schaible

Loring Schaible

Candidate

Earth and Planetary Sciences

Department

This thesis is approved, and it is acceptable in quality and form for publication:

Approved by the Thesis Committee:

Brandon Schmandt, PhD, Chairperson

Lindsay Worthington, PhD

Eric Lindsey, PhD

SEISMIC ANALYSIS OF THE UPPER & LOWER FALLS OF THE YELLOWSTONE RIVER

BY

LORING SCHAIBLE

BACHELOR OF ARTS, EARTH SCIENCES
DARTMOUTH COLLEGE, 2017

THESIS

Submitted in Partial Fulfillment of
the Requirements for the Degree of

Master of Science
Earth and Planetary Sciences

The University of New Mexico
Albuquerque, New Mexico

August, 2023

Seismic analysis of the Upper & Lower Falls of the Yellowstone River

Loring Schaible

Bachelor of Arts, Earth Sciences, Dartmouth College, 2017

Master of Science, Earth and Planetary Science, University of New Mexico, 2023

Abstract

Twelve years of concurrent hydrologic and continuous seismic data along with temporary seismic data demonstrate that the Upper and Lower Falls of the Grand Canyon of the Yellowstone River comprise a highly localized source of 0.5-5 Hz seismic energy that overwhelms anthropogenic contributions. In aggregate, seismic amplitude from 2008-2019 is linearly related to discharge with a correlation coefficient of 0.96. Repeated deviations from this linear relationship persist for 1-2 weeks prior to the date that Yellowstone Lake becomes clear of winter ice coverage. Seismic efficiency increases by ~50-250% during this period of ice-breakup, during which lake ice flows into the Yellowstone River. The increased seismic efficiency suggests more effective mechanical coupling due to impacts of ice and sediment mobilized during ice breakup. Models of waterfall development should account for the ice breakup period given that this period may be especially important to waterfall erosion.

Table of Contents

List of Figures

1 Introduction

Environmental seismology is the study of seismic signals caused by near-surface, non-tectonic processes (Cook and Dietze, 2022). The field has developed in the study of rivers, among many other phenomena and natural features. The young and growing subdiscipline of fluvial seismology emerged in 1993 when researchers demonstrated that seismometers deployed along an alpine stream were sensitive to changes in discharge (Govi *et al.*). Since that time, seismic techniques have developed as an effective means of continuously and remotely quantifying fluvial phenomena that could be difficult and possibly dangerous to observe directly. For example, seismic data have been used to recreate hydrological discharge time series (Anthony *et al.*, 2018), track the movement of a glacial lake outburst flood (Cook *et al.*, 2018), record the movement of bedload along a streambed (Roth *et al.*, 2016, 2017; Schmandt *et al.*, 2013, 2017; Hsu *et al.*, 2011, Barrière *et al.*, 2015), and track areas of extremely turbulent water flow (Goodling *et al.*, 2018). Forward models of seismogenesis due to impacts of sediments (Tsai *et al.*, 2012, Gimbert *et al.*, 2019) and turbulent water tractions on the streambed (Gimbert *et al.*, 2014, 2016) have strengthened the interpretations of fluvial seismic observations. This body of research has laid the foundation for the application of seismic techniques to the study of waterfall mechanics.

Waterfalls are locations of concentrated mechanical work in landscapes, where water and entrained sediment exert forces that carve and excavate bedrock over time. Erosion is enhanced during times of high stream power (i.e., discharge assuming local channel slope is constant), when there is also more sediment, and the forces are even greater (Scheingross *et al.*, 2017; Scheingross and Lamb, 2017). As such, these periods are

especially important to waterfall evolution. Aside from measurements of discharge and possibly sporadic sampling of sediment load, however, there are few tools available to quantify the erosional forces affecting waterfalls.

Waterfalls have received little attention with respect to seismic research, but seismic techniques may be especially well suited for studying their mechanics. Firstly, waterfalls are known sources of seismic (Rinehart, 1969; Iyer and Hitchcock, 1974; Brune and Oliver, 1959) and acoustic (Johnson *et al.,* 2006) energy. Seismic methods may also be especially effective at detecting transitions in the transport of sediment at waterfalls given that high velocity impacts of solid particles are efficient generators of seismic energy (Tsai *et al.,* 2012). While observing waterfalls directly is potentially dangerous to personnel and destructive to equipment, seismic instrumentation can be placed far from the stream channel and therefore out of harm's way. As an example, Goodling *et al.* (2018) used a single seismometer to track the location of extremely turbulent and dangerous flow 1.5 km away during the Oroville Dam Spillway Crisis. Though Goodling *et al.* (2018) studied a broken engineered structure and not a waterfall, the study proved the usefulness of seismic techniques in remotely, safely, and continuously quantifying the forces associated with water conditions that are too dangerous to observe directly. Such conditions are common at large waterfalls.

The Yellowstone River flows over two large waterfalls separated by about 0.5 km. The Upper Falls (33 m height) and Lower Falls (93 m height) mark the transition from a low-gradient to deeply incised channel known as the Grand Canyon of the Yellowstone (Figure 1). Discharge varies from less than 10 to greater than 250 m^3/s. Here I present an in depth study of the seismic signal of the Upper and Lower Falls. These waterfalls have

been the subject of limited seismic research. Rinehart (1969) was the first to observe a distinct seismic energy in the area immediately surrounding the waterfalls. Subsequent research by Iyer and Hitchcock (1974) found a distinct 2 Hz signal that persisted above background levels for several km surrounding the waterfalls. Most recently, Workman *et al.* (2014) found a correlation coefficient of 0.97 between discharge and 0.5-2 Hz energy recorded at a nearby seismometer. I expand upon this body of research using a combination of passive and active source seismological techniques. I use twelve years of nearly continuous seismic data recorded approximately one kilometer from both waterfalls to characterize their ambient signals. I use data from dozens more temporarily deployed seismometers to characterize the spatial relationship between noise and distance from the falls. I also use recordings during an active-source survey to estimate the combined force of the Upper and Lower Falls on their bases. My results collectively provide insights on the changing seismic noise conditions and spatial distribution of seismic noise near the falls. Firstly, I find that the Upper and Lower Falls of the Yellowstone comprise a highly localized source of 0.5-5 Hz energy. This energy dominates all other sources of such energy in the local environment. Second, I find that the relationship between seismic energy generation at the waterfalls and discharge is linear over many years. Third, I find that transient deviations in this linear relationship are concurrent with the ice breakup period on Yellowstone Lake and are likely caused by simultaneous increases in sediment transport. Lastly, I estimate that the Upper and Lower Falls together comprise a continuous vertical forcing of 10-100s of kN on their bases. Collectively, my results demonstrate that seismic techniques are helpful in characterizing waterfalls and the fluvial processes that shape them.

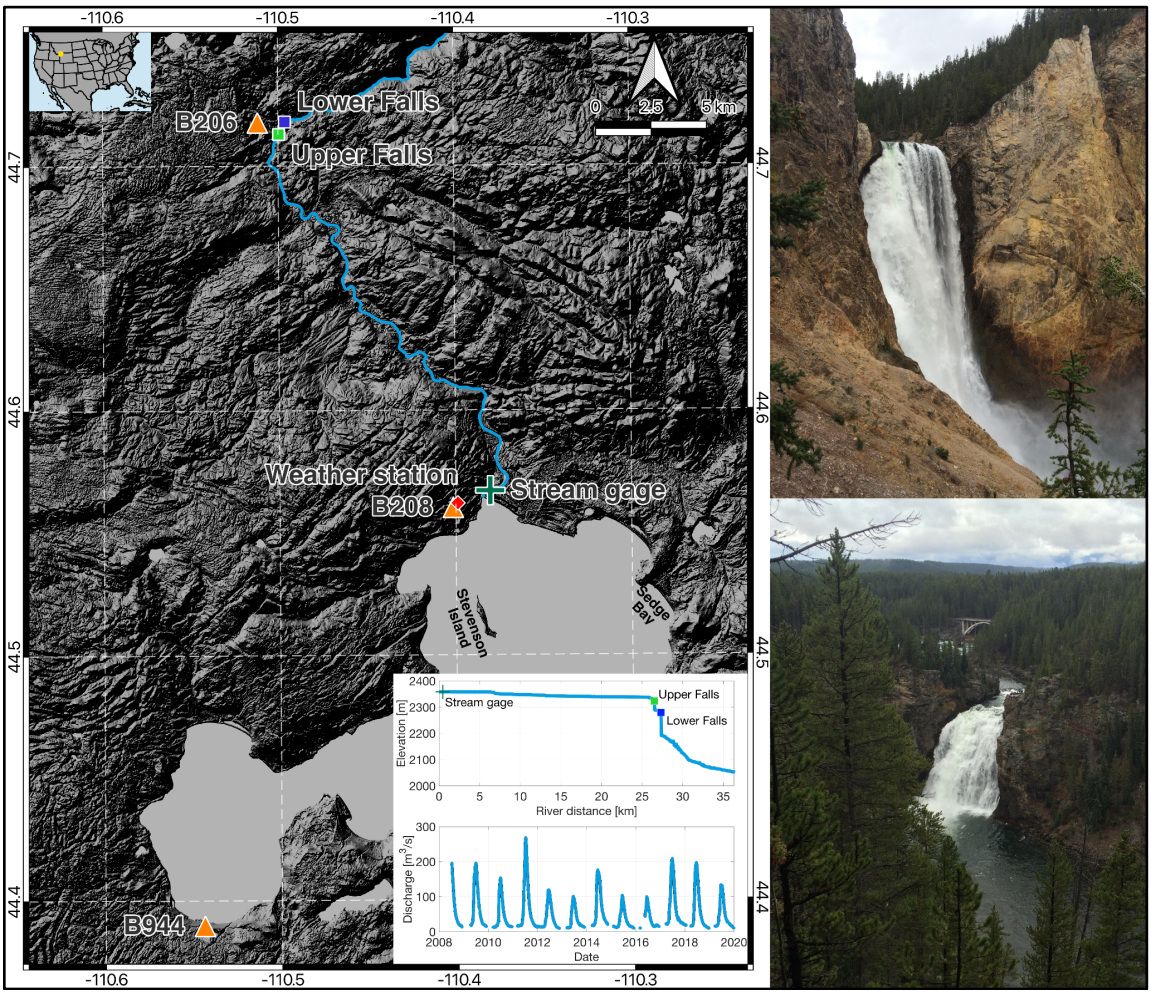

Figure 1: (Main) Map of the upper Yellowstone River from where it flows out of Yellowstone Lake, across the low-slope plains, and into the Grand Canyon of the Yellowstone starting at the Upper Falls. (Inset) (Top) Elevation profile of the Yellowstone River. (Bottom) Discharge time series from mid-2008 through 2020 as measured at the stream gage at the outlet of Yellowstone Lake. (Right) (Top) Lower Falls (Bottom) Upper Falls.

2 Data

Seismic data was collected from three permanent installations (Figure 1). Data was collected from mid-2008 through 2022 from station B206, a 74 m deep permanent borehole installation. Station B206 is 1.11 and 1.24 km from the center of the Upper and Lower Falls, respectively. For purposes of comparison with B206, data from July 2011 were collected from borehole installations B208 (163.1 m depth) and B944 (114.3 m). Data were also collected from B208 during an active Vibroseis survey in August-September 2020. The active signals were recorded at B208 from eight nearby Vibroseis survey locations (Figure 2). All three stations belong to the Plate Boundary Network and were installed in 2008. Each contains an HS-1-LT/Quanterra 330 Linear Phase Composite instrument: a 3-component geophone with a 2 Hz corner frequency and a sampling frequency of 100 Hz. Seismic data was collected from all three components as one-hour waveforms.

Figure 2: Locations of survey locations at which the Vibroseis truck emitted signals that were recorded at B208.

Seismic data was also collected from temporarily deployed seismometers, which will henceforth be referred to as the nodes. Hundreds of Fairfield Magseis Nodal seismometers containing short-period geophones with 5-Hz natural frequency and a sampling frequency of 250 Hz were deployed throughout the Park during the aforementioned Vibroseis survey. Dozens of nodes were within several km of the Upper and Lower Falls (Figure 3). Vertical data recorded between midnight and 4 am local time on August 24, 2020 was downloaded from a subset that were within several km of the Upper and Lower Falls.

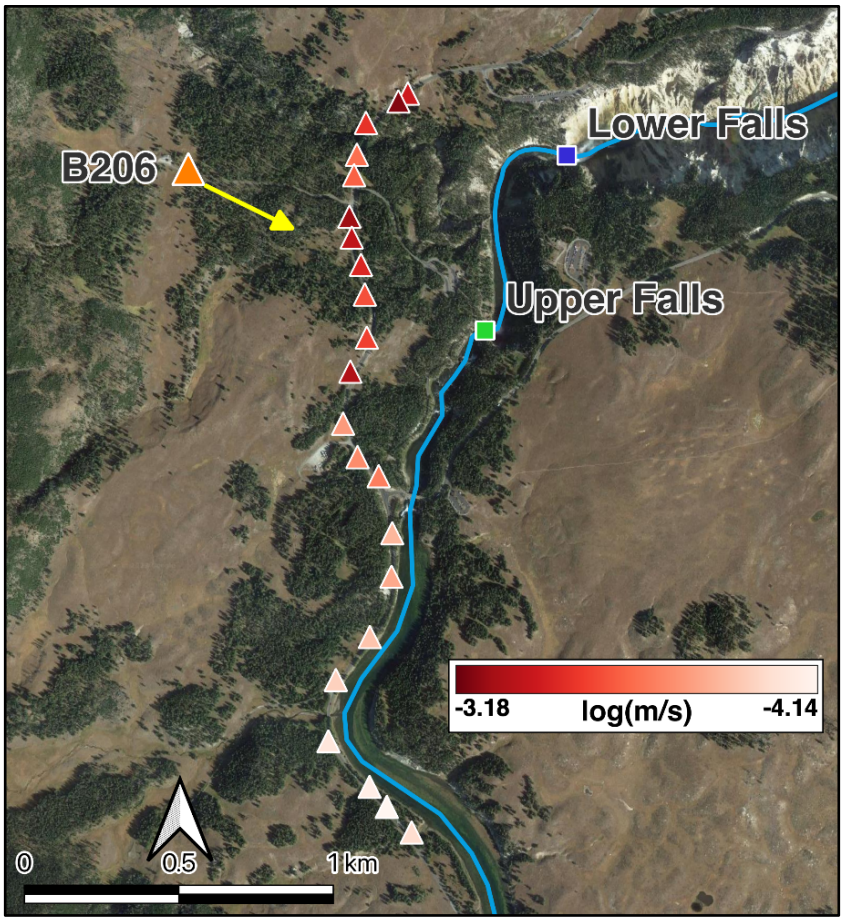

Figure 3: Locations of temporarily deployed nodal seismometers during active Vibroseis in Aug-Sept of 2020. Yellow arrow indicates the direction from which dominant energy arrives at B206.

Discharge data is derived from stage data collected at USGS gaging station 06186500 where the Yellowstone River flows out of Yellowstone Lake. While stage data is collected at varying intervals, I restrict analysis to on-the-hour measurements. Discharge is calculated according to a periodically updated empirical stage-discharge relationship. This gaging station is approximately 26 km upstream of the waterfalls and there are no major tributaries in between. There are no nearer gaging stations. The Yellowstone River's discharge is primarily driven by snowmelt input to Yellowstone Lake and is characterized by a single annual peak in discharge in early-mid summer. Discharge data was collected for the same period of record as the data available at B206. For each of the 93,118 discharge

measurements, there are accompanying one-hour seismograms for the east, north, and vertical components of B206.

Dates of ice coverage on Yellowstone Lake are collected by NPS employees and were provided by Yellowstone's Park Geologist Jeff Hungerford, PhD. The ice-off date represents the first day in each year when there is no ice observed between Sedge Bay and Stevenson Island from an overlook near Sedge Bay (pers comm. Phil Farnes).

Weather data was downloaded from the Global Historical Climatology Network daily (GHCNd) dataset. All data was recorded at the Lake Yellowstone station (USC00485345). Daily average temperature was calculated at the mean of the daily maximum and minimum. No other weather parameters were used in this study.

3 Methods

3.1 Seismic waveform processing and calculations

All raw seismic waveforms were corrected for instrument response using the following steps: means and trends were removed, waveforms were tapered, and transferred to velocity units. Seismic waveforms were rotated into true east, north, and vertical orientation for B206 only. Only vertical data was considered for all other stations. Waveforms were bandpass filtered as needed for the frequency band of interest. Power spectral densities (PSDs) were calculated using the multi-taper method (Thomson, 1982) for frequencies between 0.05 and 25 Hz for select waveforms.

I calculated median ground velocity amplitudes for all bandpassed vertical B206 waveforms. These values were calculated as the median of the absolute value of the Hilbert transform of the one-hour velocity seismogram. I calculated the same values for the nodes but over the four-hour period between midnight and 4 am local time on August 24, 2020.

Both PSD and Median vertical ground velocity amplitudes calculated for station B206 decayed over the period of record for similar discharge values. This decay revealed that the same amount of water going over the falls (i.e., force) was not causing a consistent amount of ground motion over a decadal scale. To account for this apparently changing site response and to allow for interannual comparison, velocity values were normalized to those observed in 2019. I first identified a discharge bin of 42 m^3/s +- 10%, for which there are plenty of observations for each year. I then found the median ground velocity for each year in this discharge bin and interpolated to give a correction value. This approach assumes a linear relationship between the forcing of the falling water at the surface and the

resulting ground motion. The correction factor is a number that represents how many times greater the ground motion was at that time in the discharge bin than on/after Aug 29, 2019.

3.2 Frequency dependent polarization analysis

To find from what direction the dominant energy was arriving at B206 I used frequency dependent polarization analysis (FDPA). FDPA is a technique used to characterize particle motion associated with the dominant seismic energy recorded by the receiver (Samson, 1983; Park *et al.*, 1987; Goodling *et al.*, 2018). Therefore FDPA describes the dominant rather than all motion recorded at the receiver. That is, for a seismic recording of an anisotropic field, FDPA describes the direction in which seismic energy at a given frequency is most polarized (Park *et al.*, 1987). Seismometers record particle motions in units of ground velocity. In a perfectly isotropic field, the motions recorded can be conceptualized as all fitting in an imaginary sphere whose radius is proportional to the magnitude of recorded motion. In an anisotropic field, when more energy arrives at the seismometer from some direction than others, this sphere becomes what Park *et al.* (1987) termed the 'particle motion ellipse,' whose long axis points in the direction of maximum motion.

FDPA analysis requires three-component seismic data to calculates over range of frequency values: the dominant eigenvector of the particle motion ellipsoid; degree of polarization (DOP), which ranges from 0 when all three eigenvalues are equal and one when only one eigenvalue is non-zero; the azimuth of the ellipsoid measured clockwise from North; angle of incidence from vertical; the horizontal phase angle difference; and

the vertical-horizontal phase angle difference. The parameters of interest in this study are DOP and azimuth.

I ran the FDPA analysis for 8,495 1-hour seismograms recorded at B206 between midnight and 5 AM local time for all years 2008 through 2019. I restricted the hours to the quiet nighttime hours to avoid the influence of anthropogenic noise. I calculated the mean values of DOP and azimuth over the 0.5-2 Hz, which was found to be more stable than the 0.5-5 Hz band. Azimuth calculations are uninterpretable for motion that is insufficiently polarized (Samson, 1983). I used a threshold criterion to calculate azimuth for polarizations greater than or equal to 0.6, the same value used by Koper and Hawley (2010). The results differ little from when using a value of 0.5, as in Goodling *et al.* (2018). Azimuth is also not defined if the horizontal phase angle difference is ±90±20, and so I restricted my calculations to defined values. DOP and azimuth values were calculated per discharge bin. For analyses regarding daytime, day was defined as the five-hour period starting at noon and ending at 5 pm local time. As noted in Goodling (2017), the time-averaging in FDPA diminishes the influence of transient sources of seismic energy such as earthquakes, human activity.

3.3 Seismic efficiency

I define a variable that allows for the quantification of the amount of seismic energy generated by the waterfall per unit of discharge. I define the variable 'seismic efficiency' to be the ratio of corrected bandpassed ground velocity amplitudes to discharge. Seismic efficiency is a term defined for earthquake processes but here is a measure of how discharge

couples with the Earth to generate seismic energy. Normalizing ground motion to discharge allows us to identify deviations in seismic efficiency as a function of time.

3.4 Green's function recovery and force estimation

3.4.1 Vibroseis survey

An active vibroseis survey was conducted throughout the Park in Aug-Sept 2020. During this survey, hundreds of temporary seismometers were deployed to record the active signal of the vibroseis truck, which emitted signals at specific locations. At each survey location, the truck repeated a defined sweep (signal) 20 times. Each sweep transitioned linearly from 6 Hz at the start to 30 Hz at the end of each 30 second song. During the sweep, the truck exerted a vertical-point source equal to ~220 kN (mass of truck is 24,000 kg).

Eight vibroseis survey locations were within 5.3 km of B208. For each of the eight locations, each of the 20 signals were observed as a ground velocity seismogram at B208. The recordings of the sweeps were screened for consistency for each location and any inconsistent ones were removed. The retained vibe signals were stacked and the 8-10 Hz window isolated. I calculated the mean amplitude of the 8-10 Hz window of the envelope of the stack as well as the distance between the vibroseis truck and B208 (Supplemental Figures S1 and S2).

3.4.2 Synthetic seismogram modeling

I generated synthetic seismograms using the program QSeis (Wang, 1999). This program allows the user to define the source mechanism, the source depth, receiver depth,

and the shallow earth structure. I calculated seismograms for a receiver at 163.1 m depth (same as B208) in response to a vertical forcing of 220 kN at the surface (i.e., 0 m depth). QSeis requires values of Vp, Vs, ρ, Qp, and Qs at specified depths and linearly interpolates between. I tried many different Earth structures to find one that produced estimated ground motions similar to those observed at B208. I compared the expected maximum ground motion to the observed ground motion, both in the 8-10 Hz frequency band. I defined a base model and varied Vp, Vs, Qp, and Qs for each test model. I quantified how well each test model created predictions that agreed with observation as the sum of the squares of the differences divided by the observational uncertainty, which is the Chi-squared misfit.

The base model is based on Boore and Joyner's (1997) Vs model for depths up to 8 km and the ak135f model for greater depths (Kennett *et al.*, 1995, Montagner and Kennett, 1995). Boore and Joyner's model prescribes a general Vs(z) model for depths from 0-8 km and a ρ(Vs) model. Values of Vp were calculated according to equation nine in Brocher (2005) with the Vp/Vs ratio capped at a maximum Vp/Vs of 3 (2005). Values for Qp and Qs for 0, 1 m, and 1 km depth were taken from Abercrombie (1997) and linearly interpolated in between. Values of Qp and Qs for depths greater than 1 km were taken from ak135f (Kennett *et al.*, 1995; Montagner and Kennett, 1995).

The recovery of a suitable Green's function was achieved when a suitable Earth model - one whose predictions closely resembled observations - was identified. I used the best Earth model to calculate ground velocity in the 0.5-5 Hz band for a receiver at 74.1 m depth (same as B206) in response to a 220 kN vertical forcing 1.175 km away (the mean of 1.11 and 1.24 km, the distances to the Upper and Lower Falls, respectively). I then scaled

this ground velocity per force relationship to observed ground velocities to find the force that must have produced such motion, resulting in a force time series.

4 Results

4.1 Nodal seismic amplitude vs. distance from waterfalls

Median ground velocity amplitudes in the 0.5-5 Hz band recorded at the nodes deployed along the road sub-parallel to the river exhibit rapid decay with the average distance from the Upper and Lower Falls (Figure 4). The greatest ground motion is 6.6e-4 m/s and occurs at a station that is somewhat closer to the Upper than Lower Falls. Ground velocity rapidly drops off to approximately 1/6th of that value within 1 km average distance. Discharge during this 4 hour window was steady at 45.9-46.2 m^3/s.

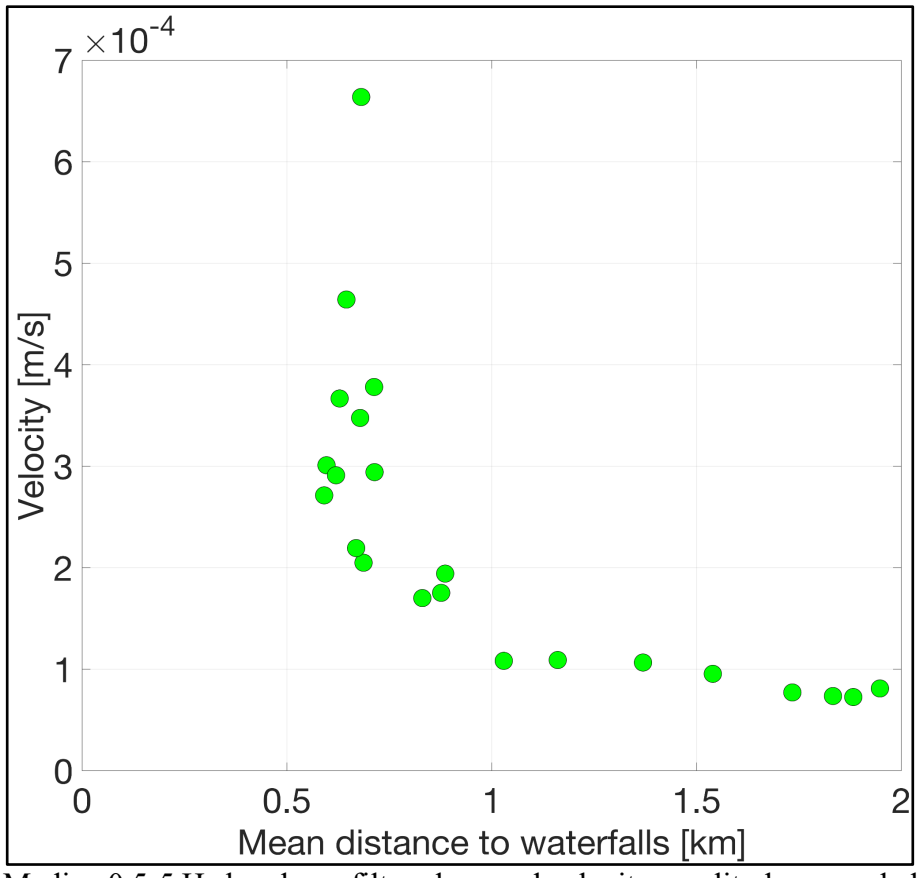

Figure 4: Median 0.5-5 Hz bandpass filtered ground velocity amplitudes recorded between midnight and 4 am on Aug 24, 2020 at a dense array of temporary seismometers deployed along the road sub-parallel to the river.

4.2 Comparison of discharge and power spectral density at B206

Power spectral density (PSD) analysis reveals that 0.5-5 Hz seismic noise recorded at B206 is sensitive to discharge (Figure 5). At moderate discharge (57-113 m^3/s) the median PSD increases ~5 dB from ~1-4.5 Hz relative to the median PSD for low discharge (<57 m^3/s). Higher discharge (>113 m^3/s) increasingly activates lower frequencies of ~0.5-1 Hz, for which there are ~25 dB increases for discharges >227 m^3/s. Above 5 Hz, the higher discharge bins do generally exhibit greater power but the differences between the highest and lowest bins are much smaller.

The distribution of most powerful frequencies also shifts to lower frequency values as discharge increases. For example, the most powerful frequency in the lowest discharge bin is centered around 3 Hz. For the greatest discharge bin, however, there is a broad range of powerful frequencies from about 1-3 Hz.

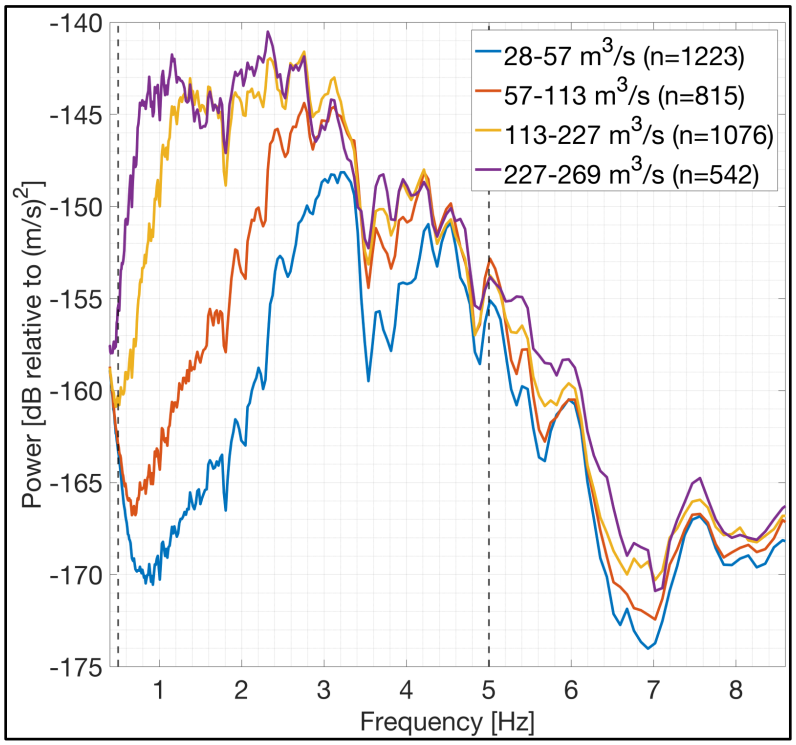

Figure 5: Median PSDs per discharge bin for 2011 only

4.3 Borehole comparison

A comparison of the median PSDs for three borehole stations in the Park shows that the ambient signal recorded at B206 does not exhibit the diurnal variation that the other two do (Figure 6). Median PSDs were calculated for each station for all available vertical seismic data in July 2011 for both day (noon-5pm) and night (midnight-5 am). Both B208 and B944 experience an increase in power over the full ~1-8 Hz band between night and day. Station B206 experiences no notable diurnal variation at any frequencies. Stations B208 and B944 are a median of 12.8 and 11.5 dB more powerful during the day in the 1-5 Hz band. Station B206 is 0.13 dB more powerful during the day, approximately 3%. Station B206 is 27.5 and 29.9 dB more powerful than B208 and B944, respectively, at night over the same band. Even during the day, B206 is 13.9 and 18.8 dB louder than B208 and B944. All three areas are heavily trafficked by tourists and have roads and other infrastructure nearby.

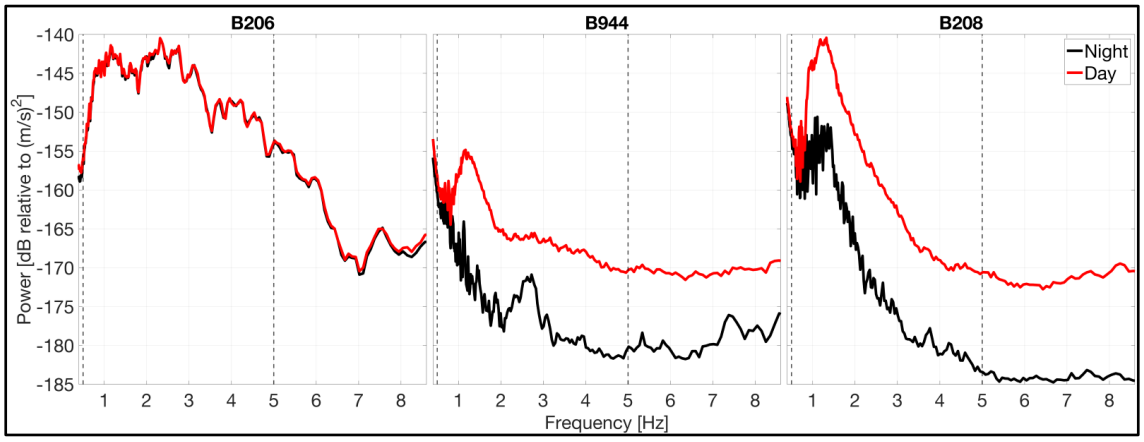

Figure 6: Median vertical PSDs for all available data in July 2011 for borehole seismometers B206, B944, and B208. The 0.5-5 Hz area is marked by dashed vertical lines.

4.4 Locating waterfall energy with FDPA

FDPA analysis of all ambient waveforms at B206 reveals a mean azimuth of 114.4 degrees for dominant seismic arrivals in the 0.5-2 Hz band. The azimuth to the Upper Falls is 119 degrees and to the Lower Falls 88 degrees. FDPA parameters grouped by discharge bins reveals that both DOP and azimuth values are consistent despite different discharge conditions (Figure 7). DOP is consistently between 0.5 and 0.7 across all bins. The lowest mean DOP occurs for the highest discharge bins and the greatest DOP for moderate discharge. Variation in DOP is similar for all but the three largest bins, which have many fewer observations. Azimuth consistently points to an area of several degrees on either side of the Upper Falls. Azimuth points south of the Upper Falls for the three highest discharge bins. Otherwise, the azimuth of dominant arrivals points to an area between the two waterfalls, as does the overall mean azimuth of 114.4 degrees. In all cases, the azimuth of dominant arrivals is closer to that of the Upper than Lower Falls. FDPA analysis focused on the narrower 0.5-2 Hz band because the 2-5 Hz band was found to be less stable. Frequencies 0.5-2 Hz are still sensitive to discharge conditions.

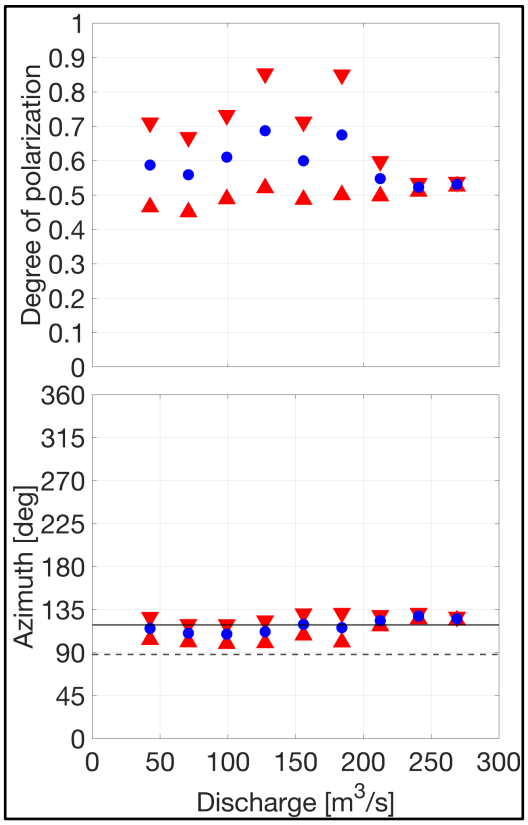

Figure 7: Frequency dependent polarization analysis of B206 for frequencies between 0.5 and 2 Hz versus discharge. (Top) Degree of polarization (Bottom) Azimuth values per discharge bin. Azimuths consistently indicate dominant arrivals in the direction of the Upper (119 degrees) and Lower Falls (88 degrees), which are marked as the solid and dashed black lines, respectively. Red triangles mark the standard deviations distance from the mean, which are blue circles. Azimuth means per bin range from 109.4 to 128.1 degrees.

4.5 Comparison of ground motion and discharge

4.5.1 Unit correction

The response of B206 to the same discharge decayed over the years of observation. Power values of the median yearly PSD in the discharge bin of 42 m^3/s +- 10% decreased over the years of the study, especially in the 1-3 Hz range (Figure 8). Expectedly, the amount of ground motion decreased for all discharge values, not just the bin of interest above (Figure 6).

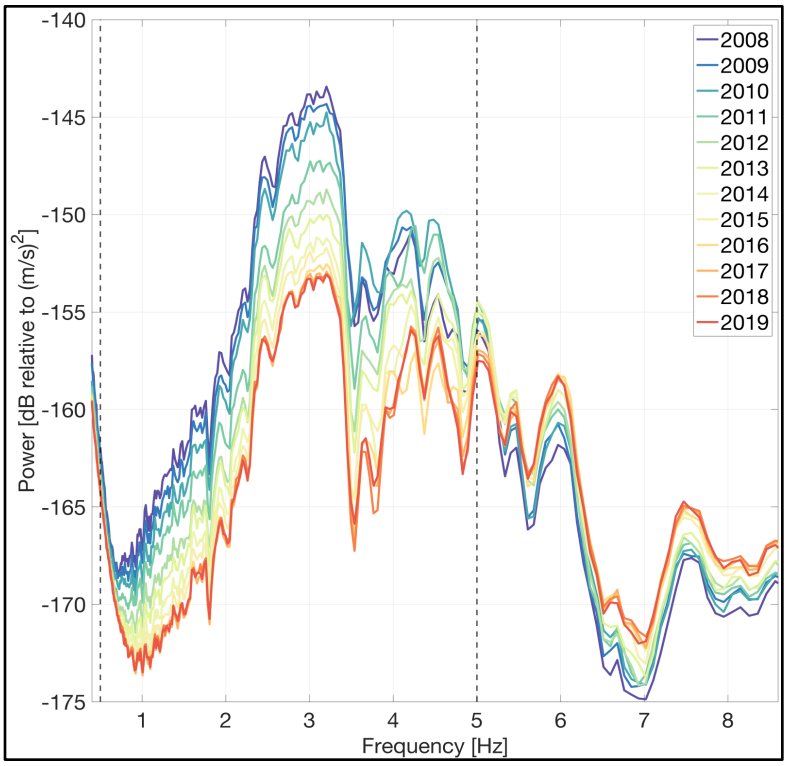

Figure 8: Median annual PSD in the 42+-10% m^3/s discharge bin

This decay was not confined to just the discharge bin above but affected all discharge levels. To account for this apparent changing site response, units were normalized to those observed in 2019 (Figure 9). First, I found the median ground velocity amplitude for each 0.5-5 Hz bandpassed 1-hour waveform. I then found the median ground velocity for each year in the 42 m^3/s +- 10% discharge bin. I then calculated a correction factor such that all median ground velocities in this bin would be the same in 2019 units. The bin 42 m^3/s +- 10% (37.8-46.2 m^3/s) is a discharge value that is reached each year with plenty of observations. The correction factor is a number that represents how many times greater the ground motion was at that time in the 42+-10 m^3/s discharge bin than on/after Aug 29, 2019. Correcting the units for the apparent decay in response gives ground velocity values that can be compared across all times in the record.

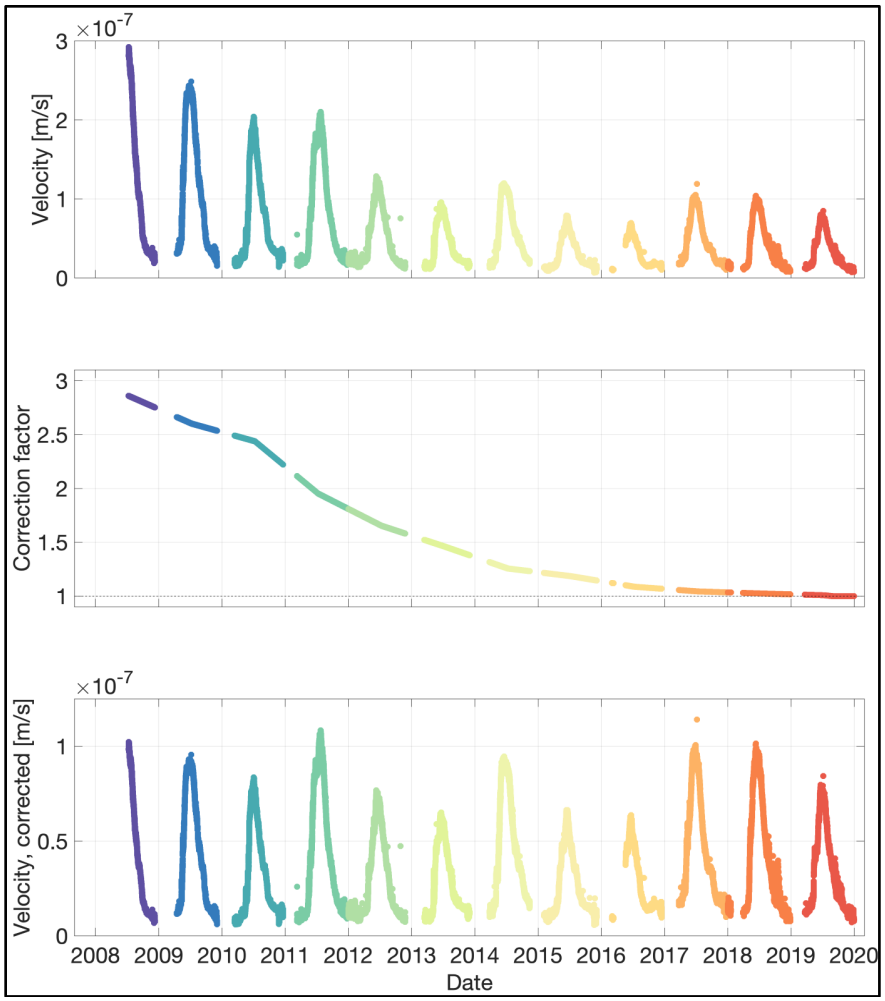

Figure 9: (Top) Uncorrected median 0.5-5 Hz bandpassed ground velocity amplitudes. (Middle) Correction factor derived by normalizing amplitudes in the 42 m^3/s ± 10% bin. (Bottom) Amplitudes corrected using correction factor.

4.5.2 Correlation between seismic amplitude and discharge

Seismic amplitude and discharge are highly linearly correlated on a per year basis before correction and in aggregate after correction (Figure 10). After correction, the cumulative data have a linear correlation coefficient of 0.964, which is similar to the coefficients observed in individual years (0.944-0.988). The mean ratio of seismic amplitude relative to discharge is 0.76 nm/s / m^3/s with a standard deviation of 0.17 and standard error of 0.0006.

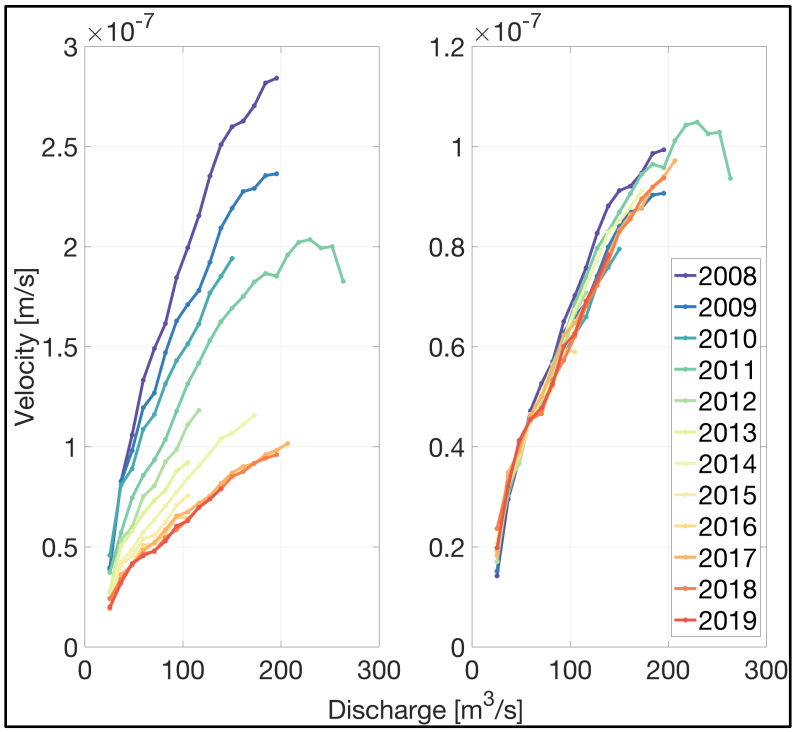

Figure 10: (Left) Uncorrected median 0.5-5 Hz bandpassed ground velocity amplitude per discharge bin. All bins are ~11.3 m^3/s wide, with the lowest bin starting at 19.8 m^3/s and the largest at 257.7 (Right) Corrected for instrument site response change.

4.5.3 Transient increases in seismic efficiency during ice breakup

I defined seismic efficiency as the ratio of seismic amplitude to discharge. Viewing seismic efficiency as a function of time allows for identifying departures from the otherwise linear relationship described above. Springtime transient increases in seismic efficiency are apparent in nine of the ten years considered, all but 2015 (Figure 11). During these transients, seismic efficiency increases by a factor of 2-3 and remains more than 2-5 standard deviations above the mean for ~5-10 days. This peak also generally precedes the ice-off date by ~5-15 days.

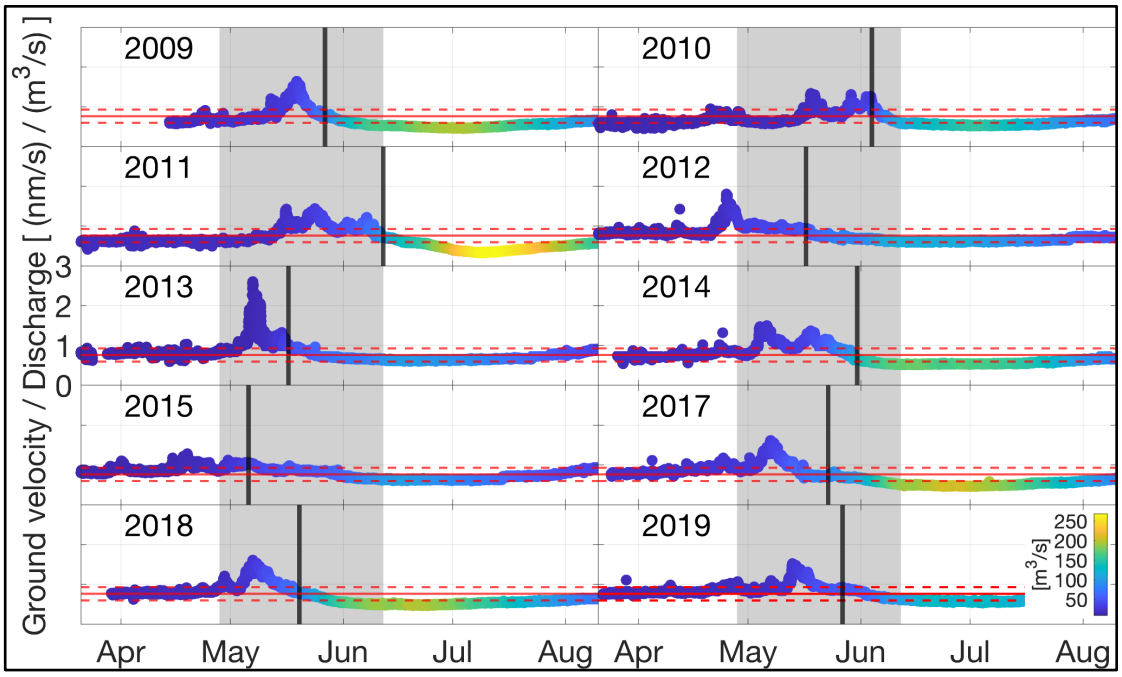

Figure 11: Corrected median 0.5-5 Hz ground velocity amplitude divided by discharge. Horizontal red lines mark the median value ±1σ. Vertical solid black line marks observed ice-off date for each year while the gray box marks the earliest and latest dates on record since 1932. Years 2008 and 2016 are excluded due to lack of data from March to August.

4.6 Force estimation

Median 8-10 Hz ground motion observed at B208 in response to the vibe signal ranged from ~33 nm/s at the nearest survey location (2.2 km) to ~2 nm/s at the furthest (5.3 km) (Figure 12). Survey locations S89 and S88 demonstrate a small deviation from an otherwise monotonically negative decay, which is expected. The observed values are compared with maximum 8-10 Hz ground motion predicted by the synthetic seismograms. The observed decay is best matched by values predicted with the Earth model whose body wave velocities at the surface are half as great as prescribed in Boore and Joyner's (1997) model. The best Earth model has P and S seismic quality factors that are 7x greater than as prescribed in Boore and Joyner's (1997) model.

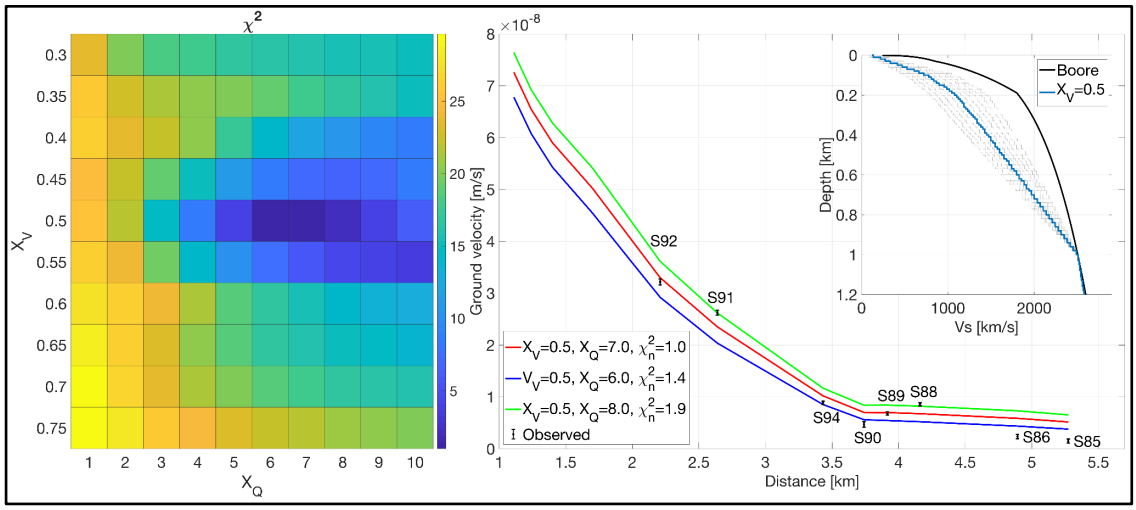

Figure 12: (Left) Tradeoff of how well various Earth models fit observed data with color indicating the normalized $\chi 2$ value. Earth models had ground velocities at the surface that ranged from 0.3 to 0.75 times that of Boore's generic model with P and S quality factor values that ranged from 1 to 10 times that of the base model. All models tested transitioned linearly into the Boore model at 1 km depth. (Right): Observed mean ground velocity at B208 in the 8-10 Hz band for each vibroseis survey station (black). Maximum amplitude of 8-10 Hz bandpassed synthetic waveforms in response to 220 kN vertical force recorded at 163.1 m depth for Earth models that best fit the observations (red, green, blue). (Inset): Depth models of all the Earth models tested with the one that best matches observed in blue.

Using the model that best produced the observations, I calculated the ground motion at 74.1 m depth in response to a station 1.175 km away from a 220 kN vertical force. A 220 kN vertical point force produces 136 nm/s of 0.5-5 Hz ground motion at a distance of 1.175 km. Given this force-motion ratio, I calculated the force timeseries of the waterfalls (Figure 13). From mid-2008 through the end of 2022, the force of the waterfalls has ranged from a minimum of ~10 to a maximum of ~170 kN. Force varies by a minimum of about an order of magnitude for each full year on record.

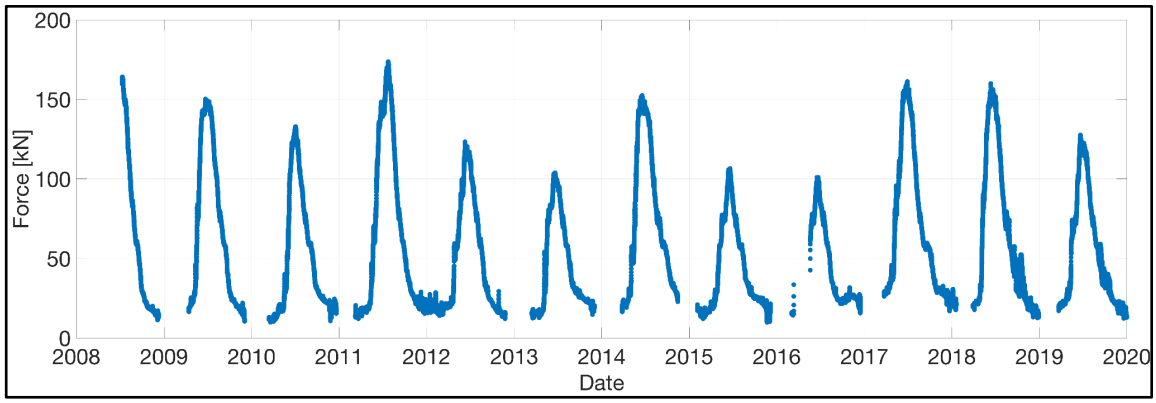

Figure 13: Force time series 2008-2020 given corrected median 0.5-5 Hz ground velocities recorded at B206.

5 Discussion

5.1 Dominance of waterfall energy at seismometer B206

The Upper and Lower Falls together comprise the source of strong 0.5-5 Hz seismic noise recorded at station B206. Firstly, the rapid decay in seismic noise at the nodes show that the waterfalls comprise a highly localized (i.e. point) source of seismic energy. Second, comparison of three borehole stations in the Park demonstrates that the waterfalls source a constant seismic noise that is ~sufficient to overwhelm anthropogenic noise. Stations B208 and B944 are sensitive to human activities, which excite frequencies across the entire ~1-8 Hz range by approximately 5-10 dB. Station B206 exhibits no such sensitivity despite the heavy traffic that frequents the area of the Upper and Lower Falls. The greater power of seismic noise at B206 across the full 0.5-8 Hz range demonstrates that the waterfalls drown out the noise due to people. Thirdly, FDPA consistently indicates a source in the direction of the Upper Falls. The FDPA azimuth vector does point between the two waterfalls though not consistently. This implies that the seismic signal of the Lower Falls does not overwhelm that of the Upper Falls even though it is ~3x taller and presumably louder. The azimuth may point more so towards the Upper Falls simply because the Upper Falls is slightly closer, which is consistent with the inverse exponential relationship between distance and seismic amplitude shown in Figure 2. I observe polarization values consistently around a value of 0.55. One might expect a more strongly polarized field given the proximity to the two waterfalls. FDPA does, however, characterize the most dominant energy, not all energy. Therefore, it may be that the presence of two strong sources at different azimuths and similar distances is enough to lower the overall polarity value. Lastly, the highly linear relationship between ground velocity amplitude at B206 and

discharge demonstrates the responsiveness of B206 to the seismic noise emanating from the falls above all other sources. This means that the cumulative effect of all other sources in the frequency band of interest must be of lesser magnitude. Consequently, I understand that the dominant source of seismic energy recorded at B206 is a combination of that originating from the Upper and Lower Falls. The dominance of the waterfalls over all other sources supports Roth *et al.*'s (2016) observation that highly turbulent flow of even small waterfalls and rapids can dominate the signals of other, nearer processes.

5.2 Seismic energy scales linearly with discharge

Ground velocity amplitudes had to be corrected for an apparent decay in response, which suggests changing conditions of the source-receiver area, the coupling of the instrument with the earth, or of the instrument itself. Diminishing amplitudes were concurrently observed for distant earthquakes of common magnitudes, indicating that the change is not a result of changes in the waterfall signals (Figure 14). Rather, the gradual change in the response of the instrument may be related to the mechanical mass-spring system itself and/or changes in coupling following borehole installation. Regardless, the unit correction provides an effective way for interannual comparison.

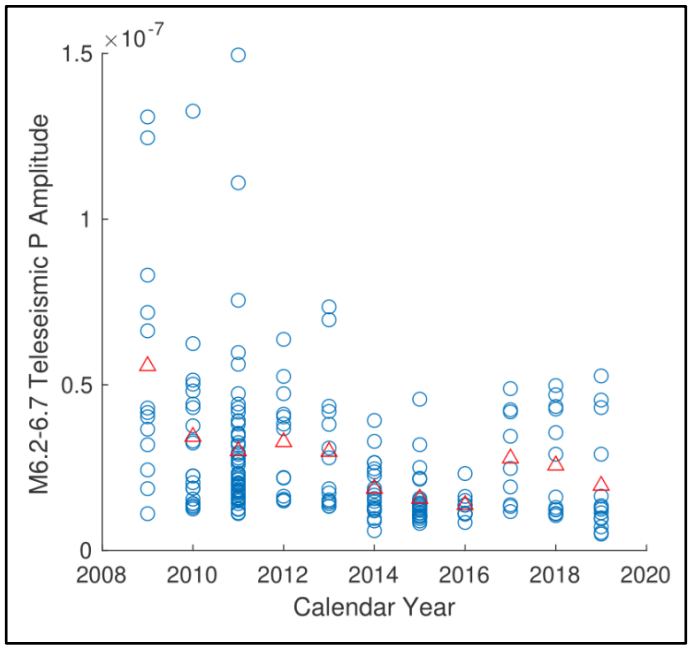

Figure 14: Teleseismic P-wave amplitudes for M6.2-6.7 events. Individual event maximum amplitudes for 204 earthquakes (blue circles) and annual mean amplitudes (red triangles) are plotted. Earthquakes are from distances of 28-92 degrees. Variability in the annual magnitude distribution (within the 6.2-6.7 range) and mechanisms of earthquake likely contribute to scatter. There is a clear amplitude decay from 2009 to 2019 that is similar to the amplitude decay observed with noise levels during low discharge times, with most decay in the first ~4-5 years and relatively stable amplitudes afterward.

The remarkably precise linear relationship between seismic amplitude and discharge is consistent with previous work. We observed correlation coefficients ranging from 0.944 to 0.988 and Workman *et al.* (2014) observed a maximum value of 0.97. As the river discharge increases, seismic amplitude at B206 increases linearly across an order of magnitude change in discharge from ~25 to ~250 m3/s. This linear dependence is consistent with a steady efficiency in the conversion of waterfall energy into radiated seismic wave energy. The total available energy per unit time (ie. power) is limited by the change in gravitational potential energy of the river's discharge. Roth *et al.* (2017) found that seismic amplitude in streams is sensitive to the arrangement of streambed sediment, which in turn affects the turbulent water flow conditions. Given that waterfalls are coupled

to their bases, Roth *et al.* suggests that any rearrangement of sediment at the base could especially affect the waterfall's seismogenesis (2017). The stability of the linear relationship discussed above and the efficiency of seismic wave generation suggests that the system is not strongly affected by discharge-dependent properties, such as the geometry of the waterfall jet or sediment content of the plunge pool.

We find preliminary evidence that the linear relationship does not hold and that decreased seismic efficiency may occur at unusually high discharge levels. Summer 2011 includes the second highest annual peak and average discharge on record since 1923. Seismic amplitude falls below the linear trend for the highest discharges observed in 2011 (>~250 m^3/s). There are fewer observations of such high discharges in the decadal dataset given their rarity. More seismic observations during discharges >250m^3/s are needed to understand this apparent deviation from the linear dependence.

Our findings are consistent with prior studies on the seismic power of fluvial systems. Seismic power (P) is related to discharge (Q) by the power-law $P \propto Q^x$. Given the linear relationship observed, the exponent is equal to 2. This value is significantly greater than 1.25 for water in an idealized channel (Gimbert *et al.*, 2014, 2016). This is expected given that falling water is coupled more strongly to the ground in the case of a waterfall than in a low-slope channel. Roth *et al.* (2017) found intermediate values of ~1.5-1.9 observed along a small channel with two small (~1 and 5 m) nearby waterfalls. Given that the observed signal is dominated by the waterfalls, it makes sense that the value found in this study is greater. The value I observe, however, is much less than those exceeding 3 observed by Goodling *et al.* (2018) during a uniquely turbulent failure of a dam spillway resulting in transport of concrete and hillslope material.

5.3 Seismic efficiency increases during ice breakup period

Positive deviations from otherwise stable seismic efficiency values indicate a change in waterfall mechanics during the ice breakup period. Large increases in sediment transport induced by the breakup and transport of ice down the Yellowstone River likely increases the mechanical coupling at the bases of the waterfalls, increasing seismic efficiency.

The Yellowstone is an ice-affected river, freezing over along some of its reaches and also transporting ice that flows out of 342 km^2 Yellowstone Lake that freezes over each winter. Ice-affected rivers are shaped by unique erosional processes. Particularly notable is the period of ice breakup, defined by Beltaos (1984) as beginning when the first sustained movement of ice occurs and ending when all residual ice has washed out of the stream. In the early stages of this transition, the ice cover on the river is weakened by rising stage, flowing water, and melting such that the ice cover breaks into rafts and chunks. While the broken pieces of ice cover are washed away, they gouge banks and beds, undercut banks, and move entrained sediment (Turcotte, 2011). These processes contribute to an ample supply of destabilized sediment that becomes part of the suspended and bedload of the river concurrent with ice breakup (Turcotte, 2011, Milburn and Prowse, 1996). This phenomenon has been observed and characterized seismically along the Sävar River, Sweden. Polvi *et al.* (2020) found elevated seismic power in frequencies consistent with bedload transport beginning during the ice breakup transition.

The observed peaks in seismic efficiency occur during times of low to moderate discharge (10-78 m3/s), not at high or peak discharge. Given that the ability of a stream to mobilize

sediments is proportional to stream power, which is in turn proportional to discharge, one would expect the peaks to occur at high and peak discharge. As noted by Beltaos and Burrell (2021), however, sediment transport during times of ice breakup can be much greater than the streams' ability to stimulate that degree of transport itself, due to the unique and efficient means of erosion. Consequently, a river may transport the majority of its annual sediment load during breakup (Vandermause, 2018). Furthermore, a river may also transport larger sediments (ie. boulders) during ice breakup than those during peak discharge (Kempena *et al.*, 2020). The ice that is transported down river and over the falls - as chunks, rafts, floes - probably contributes to the spike in seismic efficiency given that solid water couples differently to the Earth than liquid. Taken together with the knowledge that impacts of sediment clasts are efficient generators of seismic waves (Tsai *et al.*, 2012), I interpret these peaks in seismic efficiency to be attributable to ice breakup induced sediment transport over the waterfalls. Taken together, these observations suggest that ice breakup may be a particularly important window for sediment transport on the Upper Yellowstone and, consequently, waterfall evolution. This is consistent with research that suggests the breakup period may have an outsized impact on channel morphology and sediment transport (Ettema, 2002).

Existing models attribute waterfall development via downcutting to the water drilling effect of high stream power (discharge) as well as the increased capacity for erosion by sediment entrained in the stream (Scheingross *et al.*, 2017; Scheingross and Lamb, 2017). What is observed, however, is a duration of elevated seismic efficiency at times of low to moderate stream power. The increase in seismic efficiency is likely due to an increased flux of sediment, which contributes to erosion. Models that do not account for

pulses of high sediment load outside of times of high stream power would miss the importance of the ice breakup period on waterfall development.

5.4 Force estimation

To my knowledge, this is the first time the absolute force of a waterfall has been estimated. As such, there are no other published values and methods with which to compare.

In spite of having active source observations and many nearby nodes, we were unable to recover the Green's function for the area surrounding B206 because the station was offline during the vibroseis survey. Station B208 was the best available option. We assume that the Earth model parameters and Green's functions are similar for both B208 and B206. The stations are only 20 km apart and in similar geologic settings in the interior of the caldera. Their respective Green's functions, however, are undoubtedly not exactly the same.

It is clear that local observations of seismic attenuation during an active survey are essential to finding a proper Earth model with which to predict movement. The model that we found best reproduced the observed values was very different from that prescribed by Boore and Joyner (1997) for a generic site. Specifically, the body wave velocities at the surface are 0.5 times that prescribed. And the seismic quality factors are seven times greater. If we had not had the local observations of seismic attenuation afforded by the vibroseis survey and just used the generic model, our force estimates would have been very different. Lagarde *et al.* (2021) also found that local Green's function characterization is important in fluvial seismic studies.

6 Conclusions

In this project, I have used seismic techniques combined with hydrological data to demonstrate that the Upper and Lower Falls of the Yellowstone River source constant seismic energy that dominates the 0.5-5 Hz recordings of nearby seismometer B206. Using data from dozens of temporarily deployed seismometers, I also demonstrate that the Upper and Lower Falls comprise a strongly localized (i.e., point) source of 0.5-5 Hz energy. I find that seismic amplitudes at B206 exhibit a high linear correlation with discharge. Seismic efficiency, the ratio between seismic amplitude and discharge, deviates in the springtime concurrent with the period of ice breakup on Yellowstone Lake and Yellowstone River. I attribute these transient increases in seismic efficiency to erosional forces by the ice, resulting in greatly increased sediment supply and bedload transport. Greatly increased bedload is a well-documented phenomena during the period of ice breakup on ice-affected rivers. The relatively short period during which ice breaks up on Yellowstone Lake and is transported down the River likely moves a disproportionate amount of the year's sediment. Given the high erosive capacity of sediment, this short period of time may also exert an outsized influence on the morphology and evolution of the Upper and Lower Falls. Lastly, using seismic observations from an active source project, I estimated the cumulative vertical force of the waterfalls on their bases to range from 10s to 100s of kN. The force exerted on the bases of the waterfalls varies by about an order of magnitude on an intra-year basis. My results demonstrate that seismic techniques are useful in characterizing waterfalls, a fluvial system that has been largely understudied due to observational limitations.

References

Abercrombie, R. E. (1997), Near-surface attenuation and site effects from comparison of surface and deep borehole recordings. Bulletin of the Seismological Society of America, 87 (3), 731–744, doi:10.1785/BSSA0870030731.

Anthony, R. E., R.C. Aster, S. Ryan, S. Rathburn, andM. G. Baker (2018), Measuring Mountain River Discharge Using Seismographs Emplaced Within the Hyporheic Zone, Journal of Geophysical Research: Earth Surface, 123 (2), 210-228. doi:10.1002/2017JF004295.

Barrière, J., A. Oth, R. Hostache, and A. Krein (2015), Bed load transport monitoring using seismic observations in a low-gradient rural gravel bed stream, Geophysical Research Letters, 42, 2294-2301, doi:10.1002/2015GL063630.

Beltaos, S. (1984), A conceptual model for river ice breakup. Canadian Journal of Civil Engineering, 11, 516-529.

Beltaos, S. and B. C. Burrell (2021), Effects of River-Ice Breakup on Sediment Transport and Implications to Stream Environments: A Review, Water 2021, 13, 2541. doi.org/10.3390/w13182541.

Boore, D. M. and B. B. Joyner (1997), Site amplifications for generic rock sites, Bulletin of the Seismological Society of America, 87 (2), 327–341. doi:10.1785/BSSA0870020327

Burtin, A., L. Bollinger, J. Vergne, R. Cattin, and J. L. Nábělek (2008), Spectral analysis of seismic noise induced by rivers: A new tool to monitor spatiotemporal changes in stream hydrodynamics, Journal of Geophysical Research, 113 (B5): B05301. doi:10.1029/2007JB005034.

Brocher, T. M. (2005), Empirical Relations between Elastic Wavespeeds and Density in the Earth's Crust, Bulletin of the Seismological Society of America, 95 (6), 2081–2092. doi:10.1785/0120050077.

Brune, J. N. and J. Oliver (1959), The seismic noise of the earth's surface, Bulletin of the Seismological Society of America, 49 (4), 349–353. doi.org/10.1785/BSSA0490040349.

Cook, K. L., C. Anderman, F. Gimbert, B. R. Adhikari, and N. Hovius (2018), Glacial lake outburst floods as drivers of fluvial erosion in the Himalaya, Science, 362, 53-57, doi:10.1126/science.aat4981.

Cook, K. L. and M. Dietze (2022), Seismic Advances in Process Geomorphology, Annual Review of Earth and Planetary Sciences, 50 (1), 183-204.

Ettema, R. (2002), Review of alluvial-channel responses to river ice, Journal of Cold Regions Engineering, 16, 191-217.

Farnes, Phillip, Snowcap Hydrology, Bozeman, MT 59771-0691, 406-587-8393, farnes@montana.net.

Gimbert, F., V. C. Tsai, and M. P. Lamb (2014), A physical model for seismic noise generation by turbulent flow in rivers, Journal of Geophysical Research Earth Surface, 119, 2209-2238, doi:10.1002/2014JF003201.

Gimbert, F., V. C. Tsai, J. M. Amundson, T. C. Bartholomaus, and J. I. Walter (2016), Subseasonal changes observed in subglacial channel pressure, size, and sediment transport, Geophysical Research Letters, 43, 3786-3794, doi.org/10.1002/2016gl068337.

Gimbert, F., B. M. Fuller, M. P. Lamb, V. C. Tsai, and J. P. Johnson (2019), Particle transport mechanics and induced seismic noise in steep flume experiments with accelerometer-embedded tracers, Earth Surface Processes and Landforms, 44 (1), 219-41.

Gomez, B., R. L. Naff, and D. W. Hubbell (2006), Temporal variation in bedload transport rates associated with the migration of bedforms, Earth Surface Processes and Land- forms, 14, 135–156.

Goodling, P. J., V. Lekic, and K. Prestegaard (2018), Seismic signature of turbulence during the 2017 Oroville Dam spillway erosion crisis, Earth Surface Dynamics, 6, 351-367, doi.org/10.5194/esurf-6-351-2018.

Govi, M., F. Maraga, and F. Moia (1993), Seismic detectors for continuous bed load monitoring in a gravel stream, Hydrological Sciences Journal, 38 (2): 123-132, doi:10.1080/02626669309492650.

Gray, J. R., J. B. Laronne, and J. D. G. Marr (2010), Bedload-surrogate monitoring technologies, U.S. Geological Survey Scientific Investigations Report, 2010–5091.

Hsu, L., N. J. Finnegan, and E. E. Brodsky (2011), A seismic signature of river bedload transport during storm events, Geophysical Research Letters, 38, L13407, doi:10.1029/2011GL047759.

Iyer, H. M., and T. Hitchcock (1974), Seismic noise measurements in Yellowstone National Park, Geophysics, 39 (4), 389-400.

Johnson, J., J. Lees, and H. Yepes (2006), Volcanic eruptions, lightning, and a waterfall: Differentiating the menagerie of infrasound in the Ecuadorian jungle, Geophysical Research Letters, 33, doi:10.1029/2005GL025515.

Kempema, E.W., R. Ettema, and K. Bunte (2020), Anchor-ice rafting, an important mechanism for bed-sediment transport in cold-regions rivers, in River Flow 2020, Taylor and Francis, Oxfordshire, UK, August 2020.

Kennett B. L. N., E. R. Engdahl, and R. Buland (1995), Constraints on seismic velocities in the earth from travel times, Geophysical Journal International, 122, 108-124.

Koper, K. D. and V. L. Hawley (2010), Frequency dependent polarization analysis of ambient seismic noise recorded at a broadband seismometer in the central United States, Earthquake Science, 23, 439-447, doi:10.1007/s11589-010-0743-5.

Lagarde S., M. Dietze, F. Gimbert, J. B. Laronne, J. M. Turowski, and E. Halfi (2021), Grain-size distribution and propagation effects on seismic signals generated by bedload transport. Water Resources Research, 57 (4), e2020WR028700.

Milburn, D., and T. D. Prowse (1996), The effect of river-ice break-up on suspended sediment and select trace-element fluxes, Nordic Hydrology, 27(1-2), 69-84.

Montagner J.P. and B. L. N. Kennett (1995), How to reconcile body-wave and normal-mode reference Earth models?, Geophysical Journal International, 125, 229-248.

Polvi, L. E., M. Dietze, E. Lotsari, J. M. Turowski, and L. Lind (2020), Seismic monitoring of a subarctic river: Seasonal variations in hydraulics, sediment transport, and ice dynamics, Journal of Geophysical Research: Earth Surface, 125, doi:10.1029/2019JF005333.

Rinehart, J. S. (1969), Waterfall-generated earth vibrations, Science, 164, 1513-1514.

Roth, D. L., E. E. Brodsky, N. J. Finnegan, D. Rickenmann, J. M. Turowski, and A. Badoux (2016), Bed load sediment transport inferred from seismic signals near a river, Journal of Geophysical Research: Earth Surface, 121, 725-747, doi:10.1002/2015JF003782.

Roth, D. L., N. J. Finnegan, E. E. Brodsky, D. Rickenmann, J. M. Turowski, A. Badoux, and F. Gimbert (2017), Bed load transport and boundary roughness changes as competing causes of hysteresis in the relationship between river discharge and seismic amplitude recorded near a steep mountain stream, Journal of Geophysical Research: Earth Surface, 122, 1182-1200, doi:10.1002/2016JF004062.

Samson, J. C. (1983), The reduction of sample bias in polarization estimators for multichannel geophysical data with anisotropic noise, Geophysical Journal International, 75, 289-308, doi:10.1111/j.1365-246X.1983.tb01927.x.

Scheingross, J. S., D. Y. Lo, and M. P. Lamb (2017), Self-formed waterfall plunge pools in homogeneous rock, Geophysical Research Letters, 44, 200-208, doi:10.1002/2016GL071730.

Scheingross, J. S., and M. P. Lamb (2017), A mechanistic model of waterfall plunge pool erosion into bedrock, Journal of Geophysical Research: Earth Surface, 122, 2079-2104. doi:10.1002/2017JF004195.

Schmandt, B., R. C. Aster, D. Scherler, V. C. Tsai, and K. Karlstrom (2013), Multiple fluvial processes detected by riverside seismic and infrasound monitoring of a controlled flood in the Grand Canyon, Geophysical Research Letters, 40, 4858-4863, doi:10.1002/grl.50953.

Schmandt, B., D. Gaeuman, R. Stewart, S. M. Hansen, V. C. Tsai, and J. Smith (2017), Seismic array constraints on reach-scale bedload transport, Geology, 45 (4), 299-302, doi:10.1130/G38639.1.

Thomson, D. J. (1982), Spectrum estimation and harmonic analysis, Proceedings of the IEEE, 70 (9), 1055-1096, doi:10.1109/PROC.1982.12433.

Tsai, V. C., B. Minchew, M. P. Lamb, and J. P. Ampuero (2012), A physical model for seismic noise generation from sediment transport in rivers, Geophysical Research Letters, 39, L02404, doi:10.1029/2011GL050255.

Vandermause, R. A. (2018), The Role of Dynamic Ice-Breakup on Bank Erosion and Lateral Migration of the Middle Susitna River, Alaska, Master's Thesis, Department of Civil and Environmental Engineering, Colorado State University, Fort Collins, CO, USA.

Wang, R. (1999), A simple orthonormalization method for the stable and efficient computation of Green's functions, Bulletin of the Seismological Society of America, 89, 733-741.

Workman, E. J., K. D. Koper, R. Burlacu, and F. C. Lin, Seismic Energy From Waterfalls in Yellowstone National Park, Abstract S41A-4442 presented at 2014 Fall Meeting, AGU, San Francisco, CA.

Supplement

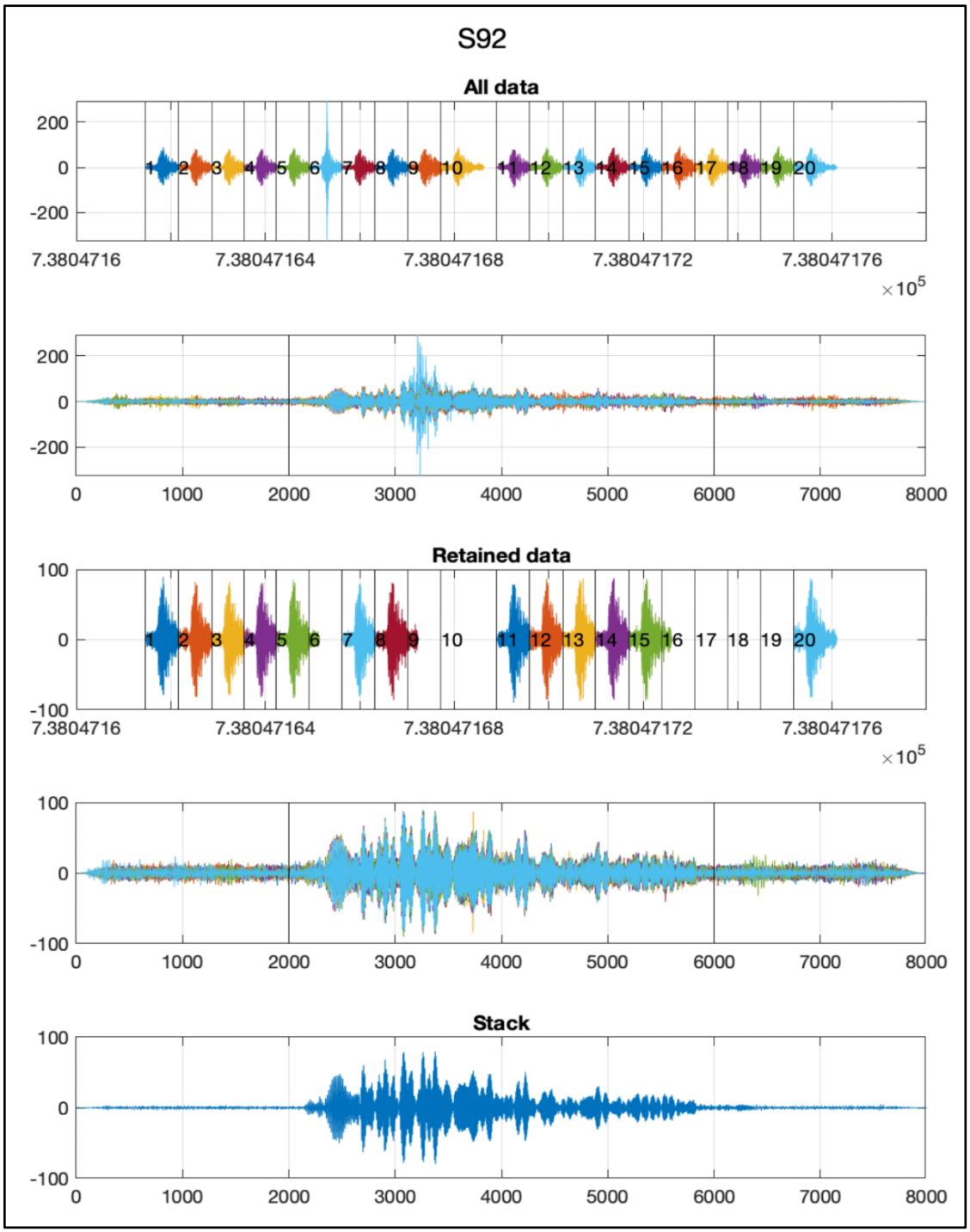

Figure S1: Screening and stacking process for the Vibroseis-induced seismograms originating at survey station S92.

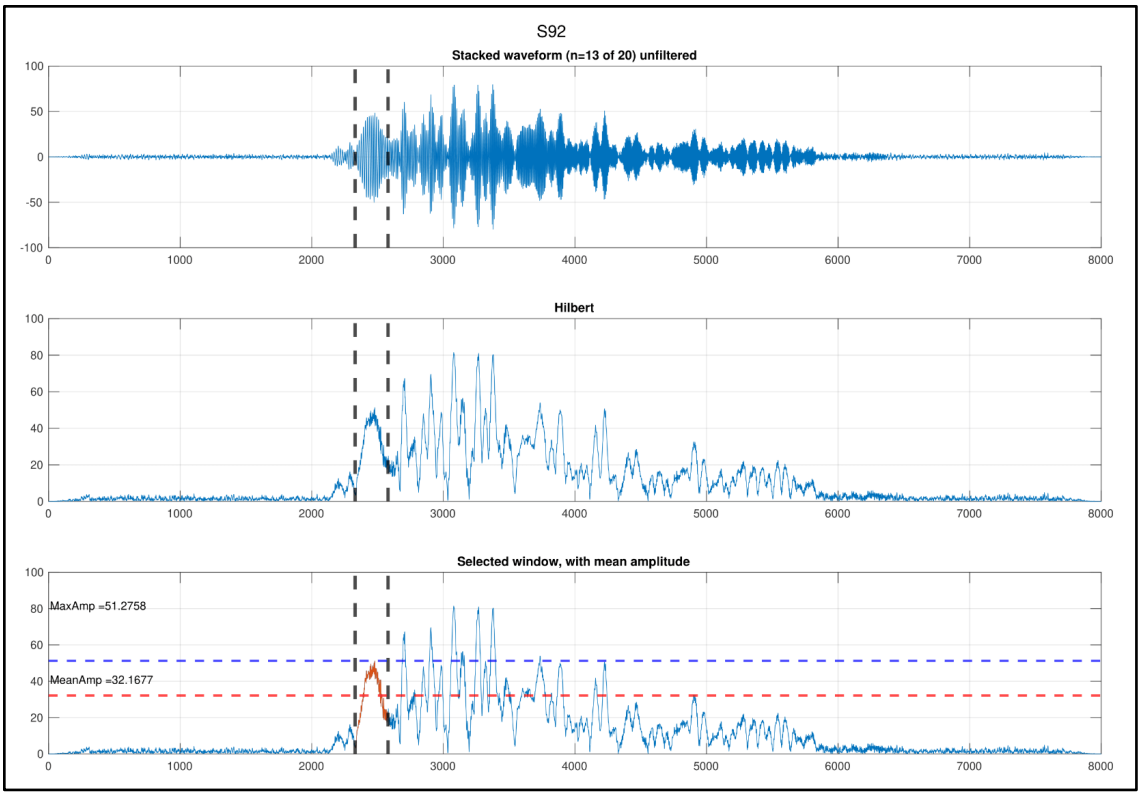

Figure S2: Estimation of 8-10 Hz ground motion amplitude in response to the Vibroseis' motion at survey station S92.

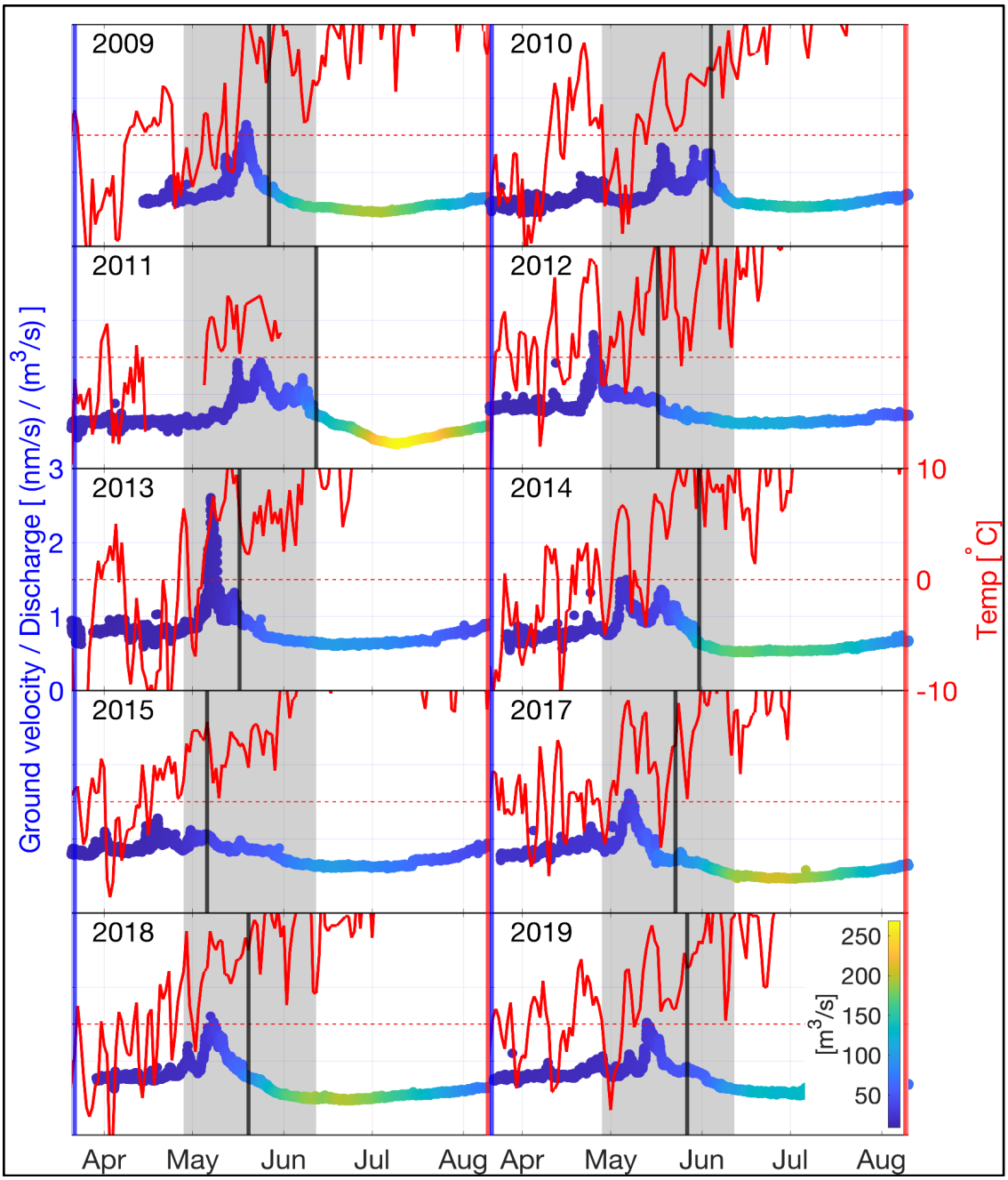

Figure S3: (Left Y-axis) Corrected median 0.5-5 Hz ground velocity amplitude divided by discharge, defined here as seismic efficiency. (Right Y-axis) Average daily temperature, 0 degrees marked by dashed horizontal red line. Vertical solid black line marks observed ice-off date for each year while the gray box marks the earliest and latest dates on record since 1932. Weather data were downloaded from the Global Historical Climatology Network daily (GHCNd) dataset for a weather station in the Park near the outlet of Yellowstone Lake.

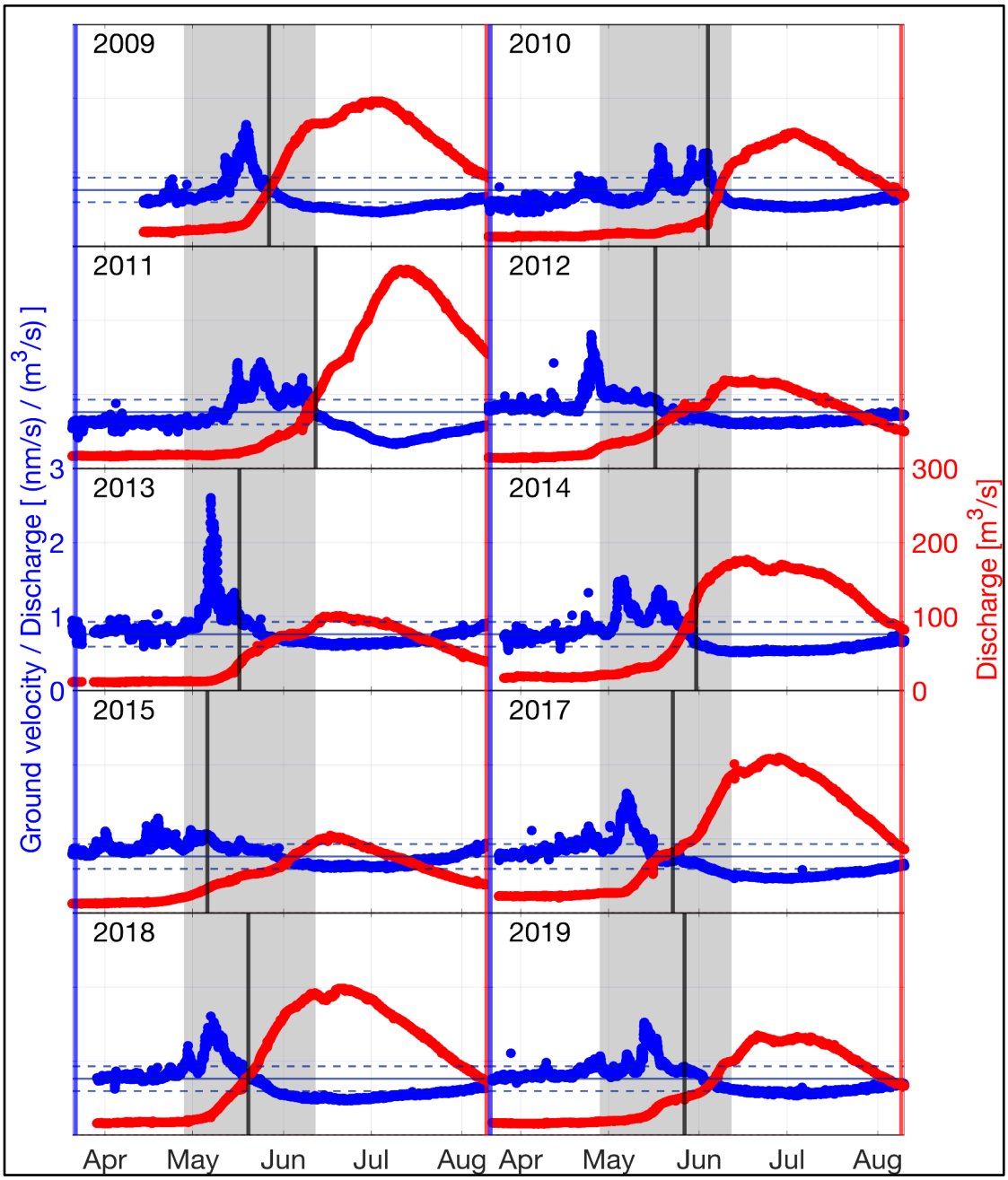

Figure S4: (Left Y-axis) Corrected median 0.5-5 Hz ground velocity amplitude divided by discharge, defined here as seismic efficiency. Horizontal black lines mark the median seismic efficiency ±1σ. (Right Y-axis) Discharge. Vertical solid black line marks observed ice-off date for each year while the gray box marks the earliest and latest dates on record since 1932.